

Shock-bubble Interaction Near a Compliant Tissue-like Material

Shusheng Pan, Stefan Adami, Xiangyu Hu, Nikolaus A. Adams*

Chair of Aerodynamics and Fluid Mechanics,
Department of Mechanical Engineering, Technical University of Munich
Boltzmannstraße 15, 85748 Garching, Germany
*nikolaus.adams@tum.de

ABSTRACT

In this work, we present numerical simulation results for shock-induced bubble collapse dynamics near tissue-like compliant gelatin phase. We use a sharp-interface model for multiple materials to represent the ambient liquid (water), the non-condensable gas phase (air) and the gelatin phase. Employing multi-resolution techniques, we investigate the complex interface dynamics and compare the results with experimental data from literature. Our aim is to understand and quantify the mechanisms observed during extracorporeal shock-wave lithotripsy or sonoporation. Therefore, late-stage dynamics of the bubble collapse and tissue penetration are presented.

INTRODUCTION

Fluid-dynamic interaction mechanisms and processes are essential to biotechnology and biomedicine (Yuan *et al.* (2015); Rooney (1970)). An important example is kidney-stone lithotripsy, side-effects of which are precursors to many other more recently proposed and pursued therapeutical approaches to improve drug delivery or to cancer treatment (Coussios & Roy (2008); Mitragotri (2005)). In medical treatment, Extracorporeal shock wave lithotripsy (ESWL) is a typical way to remove calculi in human bodies (Lingeman *et al.* (2009)). The underlying mechanism of ESWL is the shock-bubble interaction subject to various materials which leads to stone fragmentation and tissue damage (Kodama & Takayama (1998); Kodama & Tomita (2000); Loske (2010); Calvisi *et al.* (2008); Freund *et al.* (2009); Johnsen & Colonius (2009); Kobayashi *et al.* (2011)). Among the most interesting shock-interaction driven biomedical phenomena is the so-called sonoporation where acoustic cavitation of micro bubbles leads to temporary small-scale cell-membrane perforations (Fan *et al.* (2012); Prentice *et al.* (2005); Khokhlova *et al.* (2014); Zhong *et al.* (2011); Ohl *et al.* (2006)).

At the core of such processes is the generation of highly localized, bubble collapse-generated shock waves which interact with ambient fluid and tissue. This emitted shock wave is stronger than the initial impulse with orders of magnitude larger maximum pressure and hits the gelatin interface. At the same time, a liquid jet towards the interface is generated, induced by the vortical motion of the asymmetric bubble collapse. Both effects can cause a rupture of the tissue layer, however, the precise mechanisms are unclear and motivate our detailed numerical simulations.

The potential of such extremely small scale yet high-energy events enables *in situ* control of therapeutical fluid processes with high precision and minimum side effects. The eventual objective of the project of which we present here first numerical investigations is how shock interactions in life organisms can be harnessed for innovative nanoscale processes.

In this paper we present first results for a generic configuration, resembling the basic mechanism of cell-membrane poration by shock-wave impact, where a gas bubble collapse near a compliant wall is initiated by the impact of a planar shock wave. The

compliant wall is modeled as a gel-like fluid which is believed to be representative for cell-membrane material. Such setups have been studied experimentally e.g. by Kodama & Tomita (2000), here we present first results employing state-of-the-art conservative multi-material sharp-interface methods (Hu *et al.*, 2006; Han *et al.*, 2014; Pan *et al.*, 2017).

PHYSICAL MODEL AND NUMERICAL METHODOLOGY

A bubble filled with non-condensable gas is placed next to a tissue-like material and is subjected to a shock wave in water. A mixture of water and 10% solid gelatin (Kodama & Takayama (1998); Kodama & Tomita (2000)) is employed to mimic the tissue-like material, whose acoustic impedance is $1.62 \times 10^6 \text{ kg m}^{-2} \text{ s}^{-1}$, which is similar to that of many human organs, e.g., liver or kidney (Goss *et al.* (1978)). The water surrounding the gas bubble also has an acoustic impedance of $1.62 \times 10^6 \text{ kg m}^{-2} \text{ s}^{-1}$, indicating all waves are transmitted through the water-tissue interface without reflections. The material properties are listed in Table 1.

Table 1: Initial conditions and material properties.

Materials	γ	B	ρ	P	u
Air	1.4	0	1.2	P_0	0
Gelatin	4.04	6.1×10^8	1061	P_0	0
Post-shock water	4.4	6×10^8	998.6	P_0	0
Pre-shock water	4.4	6×10^8	ρ_s	P_s	u_s

The configuration is considered axi-symmetric and the stiffened equation-of-state is used for all materials. The computational domain has a length of $4R_0$ in the radial direction (x) and $80R_0$ in the axis direction (z), where $R_0 = 0.8 \text{ mm}$ is the bubble radius. The initial shock wave is located at $z = 60R_0$, $1.4R_0$ upstream of the bubble center. Its overpressure, P_s , ranges from 10.2 MPa to 163.2 MPa. The lower bound is chosen to be the same with that in an experiment (Kodama & Takayama (1998)) and the upper bound resembles pressure level observed in typical ESWL treatments Loske (2010). The exponential pressure profile, $P(z) = (P_s - P_0)e^{b(z-60R_0)} + P_0$, is the same with that in Kobayashi *et al.* (2011) and corresponds to a laser generated shock in the experiment (Kodama & Takayama (1998)). The velocity and density profile of the shock is determined by Rankine-Hugoniot relation, see u_s and ρ_s in Table 1. The surface of the tissue-like material is placed at $z = 62.4R_0$ to make sure it has attached to the downstream pole of the bubble. The chosen material properties, initial conditions and computational domain are consistent with the experiment setup (Kodama & Takayama (1998);

Kodama & Tomita (2000)) where the shock wave is generated by laser focusing and the bubble is attached to the gelatin surface using a syringe.

The Reynolds number and Weber number at the beginning of penetration in our shock-driven bubble collapse are $Re \sim O(10^5)$ and $We \sim O(10^7)$, respectively. Thus, viscous effects and surface tension effects are neglected for the tissue penetration dynamics. Other mechanisms with smaller magnitude than viscous dissipation, such as thermal diffusivity, mass diffusivity and phase change, can also be neglected (Johnsen & Colonius (2009)). For weak shock-waves with overpressure below the elastic limit, the elastic effect is initially marginal and dominates only after very large penetration. For overpressures beyond the elastic limit, the elastic effect is completely negligible. Thus we can consider the tissue penetration as a pure inertial process and treat all three materials as immiscible compressible fluids whose dynamics can be solved with our multi-material sharp interface method (Pan *et al.* (2017)).

RESULTS AND DISCUSSIONS

Verification and Validation

To demonstrate the validation of our numerical method and computational setup, we first compare our result with the experimental data for a weak shock ($P_s/P_0 = 102$). As shown in Fig. 1(a), good agreement is found for moderate penetration depths up to $L_p \simeq 2R_0$. This supports the assumption, that the penetration process is dominated by inertial effects for small and moderate deformation. At later times, the penetration decelerates significantly due to elastic effects.

Note, for large overpressures $P_s/P_0 = O(10^3)$, which are more realistic in ESWL, we expect more accurate results with our method as elastic effects are definitely negligible in this regime.

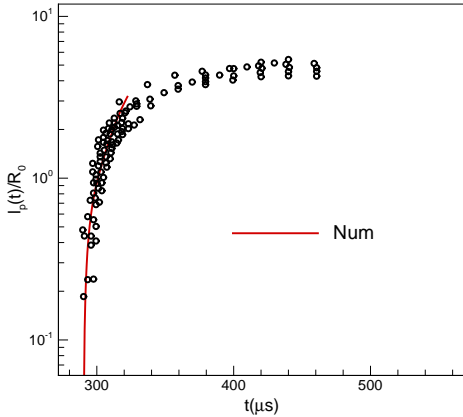


Figure 1: Comparison of simulated penetration dynamics with experimental data (Kodama & Takayama (1998); Kodama & Tomita (2000)) for $P_s/P_0 = 102$. Note, time in the simulation was adjusted to synchronize with the experiment.

Numerical convergence is verified by monitoring the temporal evolution of the equivalent bubble radius $R(t)$, i.e. the equivalent radius of a spherical bubble with the instantaneous gas bubble volume. Figure 2 shows the effective bubble radius over time during the collapse with $P_s/P_0 = 102$ for three different resolutions. Clearly, finest resolution shows converged results.

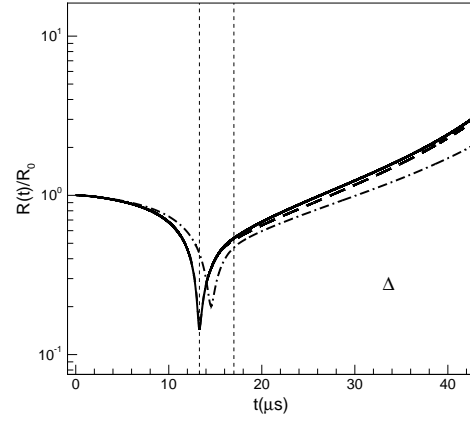


Figure 2: Equivalent bubble radius over time during a collapse simulation with $P_s/P_0 = 102$ for different grid resolutions.

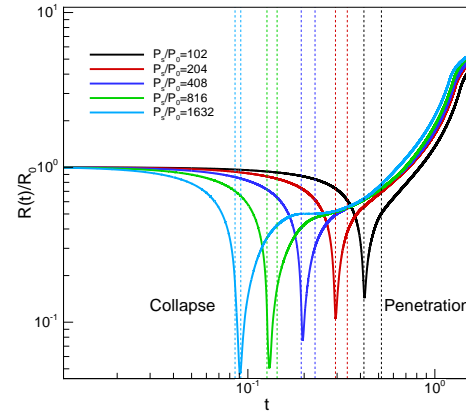


Figure 3: Time history of equivalent bubble radius during the shock-bubble interaction near a tissue-like material for various overpressures P_s/P_0 . The dashed lines show the time instant of the collapse time t_c and onset of tissue penetration.

Bubble collapse behaviour

The most distinct behaviour during the early stage of a ESWL is the shock-driven bubble collapse. The initial planar shock wave first hits the upstream pole of the gas bubble, generating a transmitted shock and a reflected rarefaction wave with different propagation directions, simultaneously. Then, the upstream interface of the bubble begins to deform. The high post-shock pressure in the water induces contraction of the gas bubble. The transient bubble collapse is shown in Fig. 3, where the equivalent bubble radius is plotted over time for various overpressures. After the strongly accelerated collapse at t_c , the bubble expands continuously. For small overpressures P_s/P_0 , the bubble reaches its minimal volume before penetrating the gelatin phase. With increasing P_s/P_0 , the onset of penetration occurs earlier and eventually happens before the collapse.

The Rayleigh collapse time of a air bubble is estimated by $t_c^R = 0.915 \sqrt{\rho_L / (P_s - P_0)} R_0$ (Brennen (2013)) for spherical collapse in free-field and $t_c^{R,*} = t_c^R (1 + 0.205 R_0 / H)$ (Vogel & Lauterborn (1988); Rattray (1951)) for non-spherical collapse near a wall,

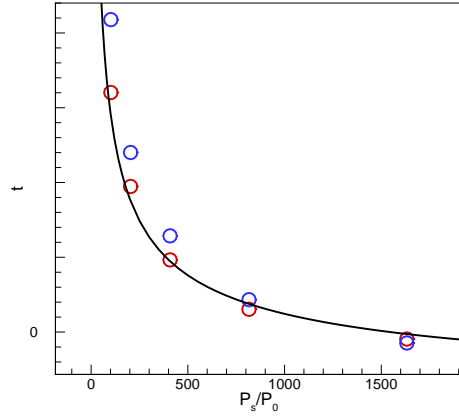


Figure 4: The bubble collapse time, t_c , as a function of pressure ratio P_s/P_0 .

where H is the stand-off distance. Due to the presence of the wall, water filling the void region generated by the collapsing bubble is missing, thus collapse is retarded (Johnsen & Colonius (2009)). As for a rigid-wall boundary, the bubble collapse near a tissue-like material is expected much slower as compared to the free-field collapse. However, given the missing “pressure doubling” effect (wave reflection at rigid wall) since acoustic impedances are identical across the tissue interface, bubble collapse in the current setup is expected even slower as compared to the non-spherical collapse near a wall. In Fig. 4, the collapse time, t_c and the onset of penetration, t_p , are shown for several pressure amplitudes. Interestingly, the collapse times are comparable to $t_c = 1.7t_c^R$, which demonstrates the slow-down of the collapse by the tissue material. Note that the collapse time for $P_s/P_0 = 102$ is $t_c = 13.3\mu s$, which agrees very well with the experimental finding of $t_c = 13\mu s$ for $P_s = 10.2$ (Kodama & Takayama (1998) (Fig. 13)). Additionally, we plotted the start times of penetration in Fig. 4. As mentioned before, at very strong shockwaves the bubble penetrates the tissue already prior collapse.

Liquid jet, shock formation and tissue surface migration

This tissue surface initially migrates towards the gas bubble due to the sink flow generated by the collapsing bubble. With increasing overpressure of the initial shockwave, this migration is smaller as the collapse time is decreasing and the sink flow effect becomes less significant. However, the migration itself is self-similar over the entire range of pressure amplitudes, see Fig. 5. Here, tissue interface migration is plotted over the rescaled pre-collapse time $(t - t_c)c_L$. The numerical data for the different overpressures can be fitted by a single quadratic function.

Usually a non-spherical bubble collapse will form a re-entrant jet due to the velocity difference of the upstream and downstream parts, $u_u - u_d$ (Blake & Gibson (1987)). For a shock-driven collapse near boundaries, the velocity u_u increases with P_s and yields large relative velocities $u_u - u_d$, indicating a strong liquid jet in shock propagation direction. This high-speed re-entrant jet will generate a water-hammer shock which propagates radially. In turn, the jet hits the tissue surface and increases the surface pressure significantly, as shown in Fig. 6. This pressure satisfies a fitting curve, $P_{w,max} = \rho_L c_L^2 [\log_w(P_s/P_0) - 2]/10$. This is of interest when measuring the potential damage of the tissue during the shock-driven bubble collapse. Note, the spatial pressure profiles along the tissue

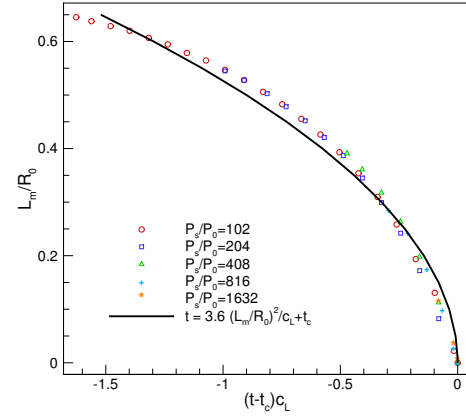


Figure 5: Migration of tissue surface during bubble collapse.

interface decrease with x (Johnsen & Colonius (2008, 2009)).

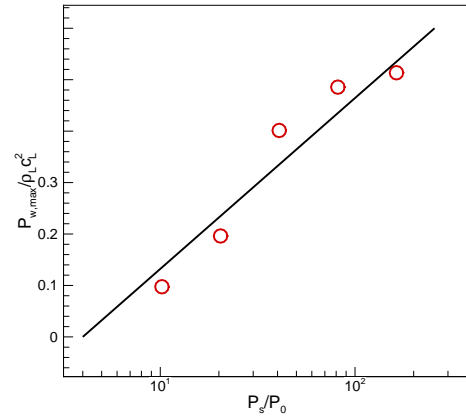


Figure 6: Maximum pressure on tissue surface at $x = 0$ as function of P_s/P_0 .

The dynamics of tissue penetration

Penetration of a continuous phase can occur when a high-speed liquid jet impacts a material, see e.g. Uth & Deshpande (2013), who investigated the unsteady water jet impact on a translucent gel experimentally. For ESWL, the shock-driven penetration is directly related to the potential damage and its dynamics remain largely unexplained.

A whole penetration process of a shock-driven bubble collapse near a tissue material is illustrated by the interface structures in Fig. 7. For larger P_s/P_0 , the penetration increases and more and more gas is convected into the tissue material. Simultaneously, the bubble elongation in vertical direction increases. The enlarged subfigure shows that the width of the liquid jet also increased with P_s significantly, which is consistent with shock-induced collapse near a wall (Johnsen & Colonius (2009)). Consequently, the amount of liquid perfusing the tissue phase increases.

Fig. 8 shows the transient tissue penetration after collapse for different overpressures P_s/P_0 . Except for late times the results are

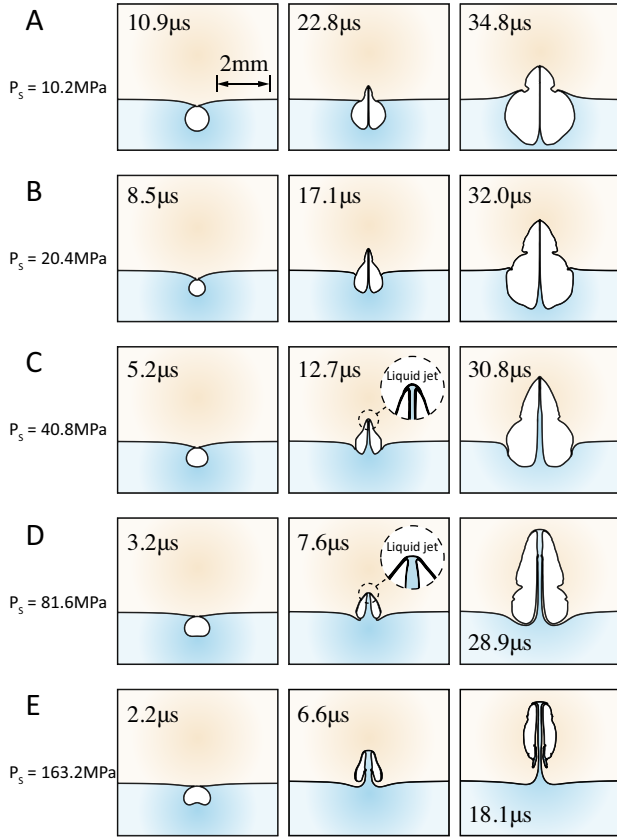


Figure 7: Snapshots of interface topology before bubble collapse (left), for small penetration depth (middle) and large penetration depth (right). The regions colored by white, yellow and blue denote air, tissue and water, respectively. The liquid jet front is enlarged to compare its thickness for different P_s .

self-similar. We derived an analytical relation for the penetration depth $L_p(t)$ as function of time using mass and momentum conservation. The resulting scaling law is given by

$$\frac{L_p(t)}{R_0} \sim \left(\sqrt{\frac{P_s \rho_G}{\rho_G^2 - \rho_L^2}} \frac{t}{R_0} \right)^{\frac{2}{3}} \sim \left(\frac{t \sqrt{P_s}}{\sqrt{\rho_L} R_0} \right)^{\frac{2}{3}} \sim \left(\frac{t}{t_c^R} \right)^{\frac{2}{3}}. \quad (1)$$

This correlation is plotted together with the simulation results in Fig. 8. The scaling law is valid from $t_p^* = 0.2$ to 4.5 and indicates a deceleration of the penetration rate. Note, the scaled penetration time is defined as $t_p^* = t / \sqrt{\rho_L P_s} / R_0$. For late times $t_p^* > 4.5$ the behavior differs as in this regime the dynamics are significantly affected by elastic forces.

Non-attached bubble collapse and penetration

So far we have studied gas bubbles attached to the gelatin interface. Now, we present results for a non-attached shock-driven bubble collapse near a tissue-like material. The stand-off distance, H , is set to $1.2R_0$ as in Kobayashi *et al.* (2011). The qualitative flow evolution with bubble collapse and tissue penetration is shown in Fig. 9. The snapshots clearly show the bubble collapse, the emitted spherical shock wave due to the water hammer event, the re-entrant liquid jet formation and the tissue penetration. Notice the multiple wave reflections and complex pressure wave pattern due to a

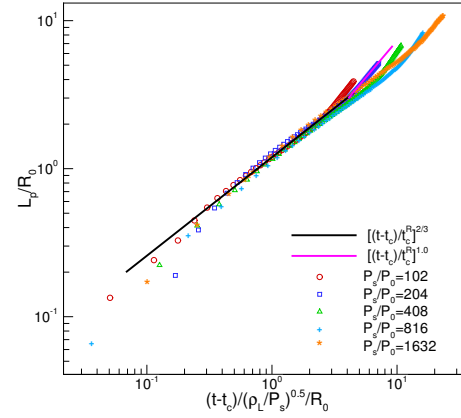


Figure 8: The penetration-time behaviour for different pressure ratio, $P_s/P_0 = 102 \sim 1632$. The scaling law is given to provide a simple model for predicting the dynamics of shock-driven tissue penetration. The time t is recorded from initial condition, not the penetration instant.

highly irregular bubble deformation. A grid convergence study for the temporal evolution of the equivalent bubble radius is shown in Fig. 10. The converged collapse time for this case is $1.6t_c^R$, which is in good agreement with the numerical result of Kobayashi *et al.* (2011) and agrees with the fitting in Fig. 4. Also, the scaled penetration depth still exhibits the same scaling law, $(t/t_c^R)^{2/3}$, see Fig. 11.

CONCLUSIONS

We have presented numerical simulations of shock-bubble interactions near a tissue-like gelatin phase using a compressible multi-material sharp-interface model. Numerical convergence was verified by grid refinement studies. We have shown that depending on the strength of the initial shockwave, the bubble can penetrate the tissue-like gelatin phase already prior maximal compression. At the same time, the strength and width of the liquid jet increases and leads to larger ambient fluid entrainment in the compliant material. A quantitative comparison of the penetration depth with experimental data from literature shows very good agreement. We found a universal scaling law for the penetration depth as a function of post-collapse time. This relation holds also for the experimental data, yet we seek for more profound validation with additional references. The numerical simulations give a detailed insight into the bubble-collapse and penetration dynamics. Different to experiments, very localized quantitative data can be extracted to understand the physical mechanisms that lead to various penetration scenarios as utilized for treatments like ESWL. More profound investigations of the liquid-jet in combination with more complex material models can help to understand and improve e.g. drug delivery into cells and are in the focus of our current research.

ACKNOWLEDGMENT

This project has received funding from China Scholarship Council (No. 201306290030) and the European Research Council (ERC) under the European Union's Horizon 2020 research and innovation programme (grant agreement No 667483). Parts of the results in this work were obtained during the CTR Summer Program 2016. The authors gratefully acknowledge the Gauss Centre for Supercomputing e.V. for funding this project by providing computing

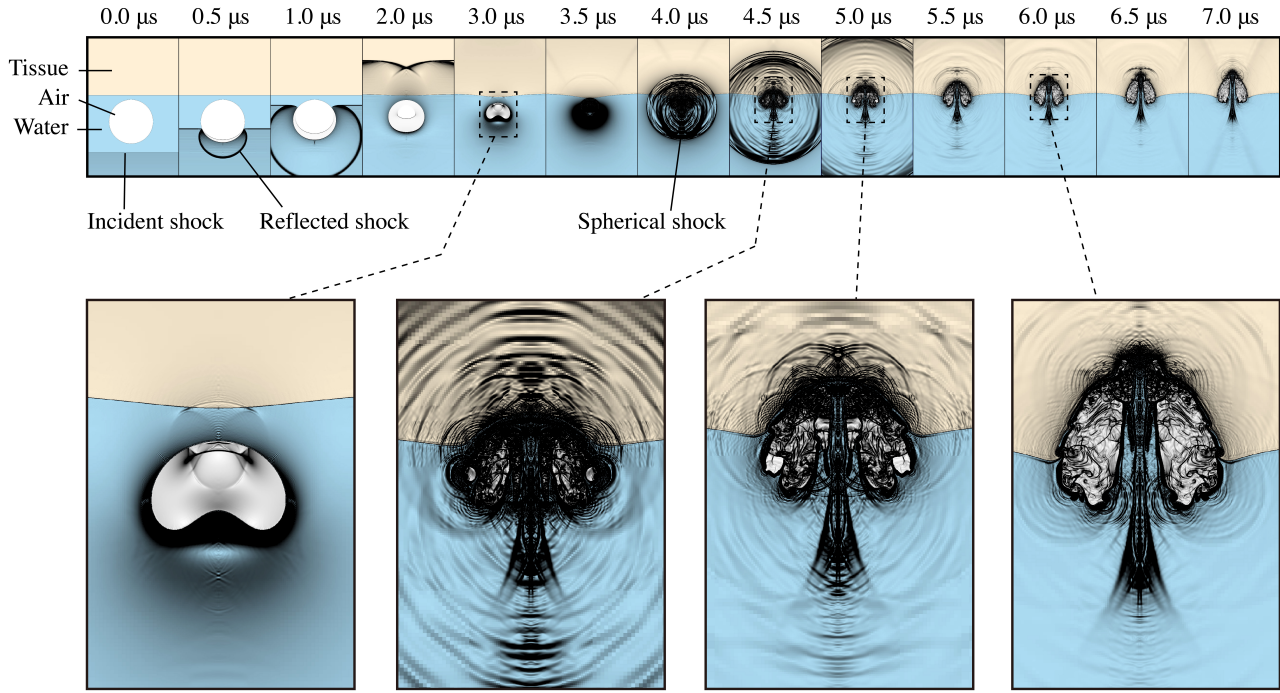


Figure 9: Bubble collapse, shock formation and tissue penetration for a non-attached bubble near a tissue-like material.

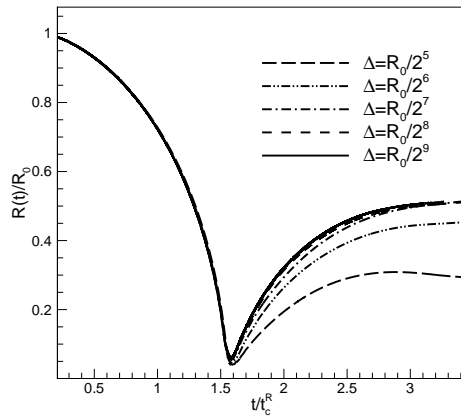


Figure 10: Equivalent bubble radius over time for a non-attached bubble with a stand-off distance $H = 1.2R_0$ and $P_s/P_0 = 1080$.

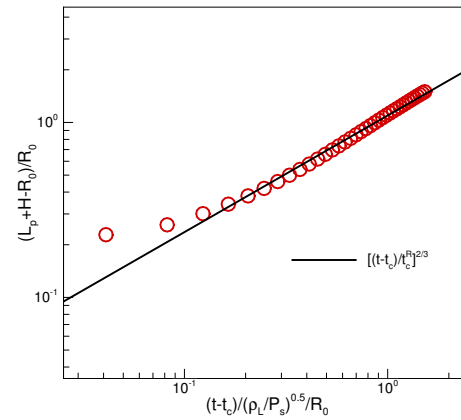


Figure 11: Tissue penetration over time for a non-attached bubble with a stand-off distance $H = 1.2R_0$ and $P_s/P_0 = 1080$.

time on the GCS Supercomputer SuperMUC at Leibniz Supercomputing Centre.

REFERENCES

- Blake, J. R & Gibson, D. C 1987 Cavitation bubbles near boundaries. *Ann. Rev. Fluid. Mech.* **19**, 99–123.
- Brennen, Christopher E 2013 *Cavitation and bubble dynamics*. Cambridge University Press.
- Calvisi, M. L., Illoreta, J. I. & Szeri, A. J. 2008 Dynamics of bubbles near a rigid surface subjected to a lithotripter shock wave. Part 2. Reflected shock intensifies non-spherical cavitation collapse. *J.*

Fluid Mech. **616**, 63.

- Coussios, Constantin C. & Roy, Ronald A. 2008 Applications of Acoustics and Cavitation to Noninvasive Therapy and Drug Delivery. *Ann. Rev. Fluid Mech.* **40** (1), 395–420.
- Fan, Zhenzhen, Liu, Haiyan, Mayer, Michael & Deng, Cheri X 2012 Spatiotemporally controlled single cell sonoporation. *Proceedings of the National Academy of Sciences* **109** (41), 16486–16491.
- Freund, J. B., Shukla, R. K. & Evan, A. P. 2009 Shock-induced bubble jetting into a viscous fluid with application to tissue injury in shock-wave lithotripsy. *The Journal of the Acoustical Society*

- of America **126** (5), 2746.
- Goss, SA, Johnston, RL & Dunn, Fry 1978 Comprehensive compilation of empirical ultrasonic properties of mammalian tissues. *The Journal of the Acoustical Society of America* **64** (2), 423–457.
- Han, L. H., Hu, X. Y. & Adams, N. A. 2014 Adaptive multi-resolution method for compressible multi-phase flows with sharp interface model and pyramid data structure. *Journal of Computational Physics* **262**, 131–152.
- Hu, X.Y., Khoo, B.C., Adams, N.A. & Huang, F.L. 2006 A conservative interface method for compressible flows. *J. Comput. Phys.* **219** (2), 553–578.
- Johnsen, Eric & Colonius, Tim 2008 Shock-induced collapse of a gas bubble in shockwave lithotripsy. *J. Acoust. Soc. Am* **124** (4), 2011–2020.
- Johnsen, Eric & Colonius, Tim 2009 Numerical simulations of non-spherical bubble collapse. *J. Fluid Mech.* **629**, 231.
- Khokhlova, Tatiana D, Wang, Yak-Nam, Simon, Julianna C, Cunitz, Bryan W, Starr, Frank, Paun, Marla, Crum, Lawrence A, Bailey, Michael R & Khokhlova, Vera A 2014 Ultrasound-guided tissue fractionation by high intensity focused ultrasound in an in vivo porcine liver model. *Proceedings of the National Academy of Sciences* **111** (22), 8161–8166.
- Kobayashi, Kazumichi, Kodama, Tetsuya & Takahira, Hiroyuki 2011 Shock wavebubble interaction near soft and rigid boundaries during lithotripsy: numerical analysis by the improved ghost fluid method. *Phys. Med. Biol.* **56** (19), 6421–6440.
- Kodama, Tetsuya & Takayama, Kazuyoshi 1998 Dynamic behavior of bubbles during extracorporeal shock-wave lithotripsy. *Ultrasound in Medicine and Biology* **24** (7), 723–738.
- Kodama, T. & Tomita, Y. 2000 Cavitation bubble behavior and bubble shock wave interaction near a gelatin surface as a study of in vivo bubble dynamics. *Applied Physics B* **70** (1), 139–149.
- Lingeman, J. E, McAteer, J. A, Gnessin, E & Evan, A. P 2009 Shock wave lithotripsy: advances in technology and technique. *Nat. Rev. Urol.* **6**, 660–70.
- Loske, A. M 2010 The role of energy density and acoustic cavitation in shock wave lithotripsy. *Ultrasonics* **50**, 300–5.
- Mitragotri, Samir 2005 Healing sound: the use of ultrasound in drug delivery and other therapeutic applications. *Nature Reviews Drug Discovery* **4** (3), 255–260.
- Ohl, Claus-Dieter, Arora, Manish, Ikink, Roy, de Jong, Nico, Versluis, Michel, Delius, Michael & Lohse, Detlef 2006 Sonoporation from Jetting Cavitation Bubbles. *Biophys. J.* **91** (11), 4285–4295.
- Pan, Shucheng, Han, Luhui, Hu, Xiangyu, Adams, Nikolaus *et al.* 2017 A conservative sharp-interface method for compressible multi-material flows. *arXiv preprint arXiv:1704.00519*.
- Prentice, Paul, Cuschieri, Alfred, Dholakia, Kishan, Prausnitz, Mark & Campbell, Paul 2005 Membrane disruption by optically controlled microbubble cavitation. *Nature physics* **1** (2), 107–110.
- Rattray, Maurice 1951 Perturbation effects in cavitation bubble dynamics. PhD thesis, California Institute of Technology.
- Rooney, James A 1970 Hemolysis near an ultrasonically pulsating gas bubble. *Science* **169** (3948), 869–871.
- Uth, Tobias & Deshpande, Vikram S 2013 Unsteady penetration of a target by a liquid jet. *Proceedings of the National Academy of Sciences* **110** (50), 20028–20033.
- Vogel, A & Lauterborn, W 1988 Acoustic transient generation by laser-produced cavitation bubbles near solid boundaries. *The Journal of the Acoustical Society of America* **84** (2), 719–731.
- Yuan, Fang, Yang, Chen & Zhong, Pei 2015 Cell membrane deformation and bioeffects produced by tandem bubble-induced jetting flow. *Proceedings of the National Academy of Sciences* **112** (51), E7039–E7047.
- Zhong, Wenjing, Sit, Wai Hung, Wan, Jennifer M.F. & Yu, Alfred C.H. 2011 Sonoporation Induces Apoptosis and Cell Cycle Arrest in Human Promyelocytic Leukemia Cells. *Ultrasound Med. Biol.* **37** (12), 2149–2159.